

# Towards a more accurate characterization of granular media: extracting quantitative descriptors from tomographic images

Ivan Vlahinić · Edward Andò · Gioacchino Viggiani · José E. Andrade

Received: 5 September 2012 / Published online: 7 December 2013  
© Springer-Verlag Berlin Heidelberg 2013

**Abstract** Imaging, epitomized by computed tomography, continues to provide unprecedented 3D access to granular microstructures at ever-greater resolutions. The non-destructive technique has enabled deep insight into the morphology and behavior of granular materials, in situ and as a function of macroscopic states, e.g., loads. However, a significant bottleneck in this paradigm is that it ultimately yields qualitative ‘pictures’ of microstructure. Hence, a major challenge is to extract *quantitative* descriptors of grain-scale processes, e.g., morphological description of particles, kinematics, and spatial interactions. Existing methods, including watershed and burn algorithms, are plagued with limitations related to image resolution and with the inability to sharply identify grain-to-grain contact regions, which is crucial for studying force transmission and strength in granular materials. In this work, we propose a method to overcome these drawbacks. Specifically, a novel way to extract grain topology in particulate materials via level sets is introduced. It is shown that the proposed method can sharply resolve the topology of grain surfaces near to and far from grain-to-grain contact regions with sub-voxel resolution, and is capable of grain extraction directly in three dimensions. The proposed method still relies on traditional techniques for input, but ultimately leads to much improved grain characterization. We validate the approach using three dimensional CT images of highly rounded (Caicos ooid) and highly angular (Hostun sand) natural materials, with excellent results.

**Keywords** Computed tomography · Level set · Granular · Discrete · Characterization · Images

## 1 Introduction

High-resolution imaging continues to provide unprecedented access into the 3D microstructure of natural granular materials. X-ray Computed Tomography (XRCT) has emerged as the most prevalent technique due to its tremendous potential to image opaque materials whose microstructure has historically been difficult to access [1, 16]. Attainable resolutions are quickly improving, with individual voxels beginning to break a micrometer lengthscale using commercially available scanners. Other techniques are able to reach much lower scales (e.g., scanning electron microscopy, scanning laser confocal microscopy) but are typically limited to surface measurements in opaque materials.

The ability to perform in situ characterization of materials has been one of the early drivers of XRCT. Here, in situ characterization refers to the extraction of morphological information in the natural state of the material. In granular materials, such extraction can yield properties available using traditional lab techniques, e.g., porosity or grain size distribution, as well as those often unavailable in practice, e.g., particle orientations and coordination numbers [39]. For example, characterization of in-situ pore space geometries has enabled numerical studies of transport properties (e.g., permeability), of importance in applications ranging from filtration to flow characteristics of hydrocarbon reservoirs [37, 38, 42].

Coupled with a loading apparatus, XRCT also enables an uninterrupted sequence of 3D snapshots, each containing thousands of grains, to be collected over the course of a single experiment. Comparing successive snapshots gives insight into the incremental microstructural changes as a function of

---

I. Vlahinić · J. E. Andrade (✉)  
InSight Mission, Jet Propulsion Laboratory,  
Pasadena, CA 91109, USA  
e-mail: jandrade@caltech.edu

E. Andò · G. Viggiani  
Grenoble-INP / UJF-Grenoble 1 / CNRS UMR 5521,  
Laboratoire 3SR, 38041 Grenoble, France

an external state (e.g., loads). Unlike at any point in history, this experimental process has opened up significant opportunities in relating discrete microstructural features to continuum macroscopic quantities [4, 11, 29]. The process has also helped steer the research focus from phenomenological towards more physics-based, with the promise of validating and improving models for granular media, and just as importantly, unmasking the physical origins of observed phenomena such as shear bands [5, 33].

A significant challenge in applying imaging such as XRCT as a general paradigm is in translating what are essentially three dimensional photographs (voxelated images) into ‘quantities’ that are palatable for mechanical analysis. In other words, the photographs need to be converted into quantitative descriptors of particle morphology and kinematics that can then be used in quantitative analysis. This necessary step not only brings image data into the physical scale of interest but also helps reduce what are extremely large data sets into a smaller set of geometric and/or statistical descriptors.<sup>1</sup> A key difficulty lies in irregularity of individual particles and also in the fact that particles are touching.

Current techniques do relatively well in segmenting grains from the pores, and also grains from other grains, i.e., discriminating grains from voids and identifying grains as individual units. However, these techniques also contain two crucial shortcomings. (1) Grain characterization is voxel-based. This unnecessarily limits the level of detail that can be extracted from 16-bit CT image data. (2) Segmentation process tends to ‘damage’ the resolution near grain-to-grain contacts. This is problematic because contact regions are of great importance to our understanding of force transmission in granular media. Both of these issues are a direct consequence of the current methods being dependent on voxelated data structures.

In this work, we overcome these shortcomings and in this way provide substantial improvements to the current characterization methods of granular materials. To improve grain boundary detection, we introduce and improve upon a level-set based method [12, 26, 31] that is free from voxelated structures, and rather works directly on greyscale XRCT images to translate these to continuum descriptions of particle morphology. Image gradients are used as ‘markers’ of grain boundaries [23, 32]. The proposed method is ultimately able to resolve grain morphology robustly and autonomously, it is not tied to the underlying image grid, and it leads to smooth surfaces that are continuously differentiable. We verify the method on two very different types of granular materials imaged using XRCT: Caicos ooids (highly rounded grains) and Hostun sand (highly angular grains) with excellent results.

<sup>1</sup> To provide a sense of scale, the images utilized in this work contain roughly one particle for every 8,000 greyscale voxels of data.

The contribution is presented in the following order: Sect. 2 reviews the background on XRCT capture, 3D image reconstruction, and current techniques for grain extraction. Section 3 provides a birds-eye view of the proposed methodology, with algorithmic details given in Sect. 4. Section 5 presents the results. Concluding remarks are offered in Sect. 6.

Finally, we note that the proposed work is applicable beyond the geomaterials discussed in this work. The need to separate individual material phases can also be found, for example, in metals that have grains and/or inclusions within range of XRCT resolution [40], with well documented importance of grain-to-grain boundaries in controlling the macroscale plasticity. Other possible applications are the segmentation of powders, fractures, or in general, systems in which one desires to quantify discrete features within a microstructure.

## 2 Background & motivation: CT capture and segmentation

### 2.1 From X-rays to stair-step grains

XRCT is revolutionizing the field of experimental mechanics due to its ability to image the microstructure in opaque materials. Particularly promising is the ability of XRCT to capture a sequence of images of a deforming material, non-destructively, with the promise of quantifying the microstructural origins of macroscale phenomena.

Despite the aforementioned goal, XRCT still yields a series of images that must ultimately be converted into mathematical ‘quantities’. A continuing challenge is the development of robust tools that are able to perform the conversion autonomously and consistently, without significant user input. Figure 1 provides a visual schematic of key non-trivial steps involved in the traditional methods. Their brief description is given next.

During the experimental process, 2D radiographs are acquired while the sample is slowly rotated. The 3D image is reconstructed, slice by slice (slices are normal to the rotation axis), from 2D radiographs at different angles by solving the inverse problem of the Radon transform. The result is a greyscale 3D image of X-ray intensities at a given material state (3DXRCT), where higher X-ray attenuation signal corresponds to denser material volumes.

After 3D image reconstruction, material phases are separated via thresholding, usually based on certain limiting criteria [35]. One such criterion used in this work is a posteriori measure of sample density—which helps preserve overall mass during thresholding. The outcome of this step (in two-phase media) is a binary image, with 1s representing the solid

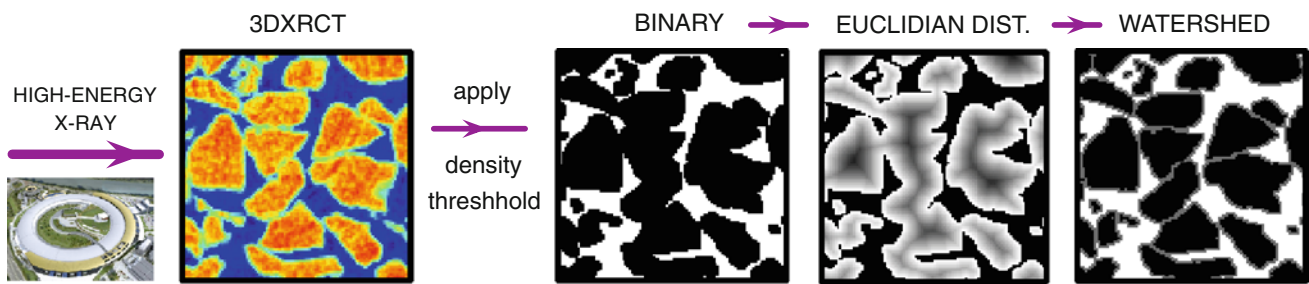


**Fig. 1** Visual schematic of the current state-of-the-art in identifying individual grains from 3D X-Ray Computed Tomography (3DXRCT) images. The reader is referred to Sect. 2.1 for a detailed discussion of the steps involved

phase and 0s the void phase. Individual grains have not yet been identified.

A single interconnected grain mass (a collection of solid voxels) is split into individual grains using a watershed-based algorithm [36]. The algorithm has been around since the 1980s, with several robust variants. The version utilized in this work is similar to that of [39], initialized by a distance map (Euclidian or otherwise) between the solid voxels and phase boundaries. Grain identification begins with the search for local maxima or islands in the distance map. Individual islands are assumed to be grain centers that are subsequently expanded. Where neighboring islands meet, a local watershed line is drawn, representing a grain-to-grain boundary.

The ultimate output of the previously described sequence steps is shown in the rightmost image of Fig. 1, where black and white colors indicate grain and void voxels, and grey are the voxels at phase/grain boundaries. For well rounded Caicos ooids with narrow distribution of particle sizes, authors’ experience indicates that watershed-based algorithm is able to detect individual grains roughly 95 % of the time. ‘Difficult’ configurations that result in lower segmentation success rates include and are not limited to: wide grain size distribution, irregular grain shapes, irregular grain-to-grain contacts, porous grains. These factors lead to either excess or shortage of the starting islands, and ultimately to an incorrect segmentation. Steps can be taken to improve the success rate, by fine-tuning starting island configurations, the speed of ‘island growth’, or both, often via trial and error.

### 2.2 Drawbacks of binary grain representation

The discrete nature of granular materials and the irregularity of grain surfaces pose significant challenges to grain segmentation. Figure 2 illustrates this point, via a histogram of X-ray intensities of angular Hostun sand. Specifically, the figure shows that for any segmentation algorithm, a major challenge is to correctly allocate a significant volume of the material (green distribution) between different material phases. For Hostun sand, the area of under the green distribution adds up

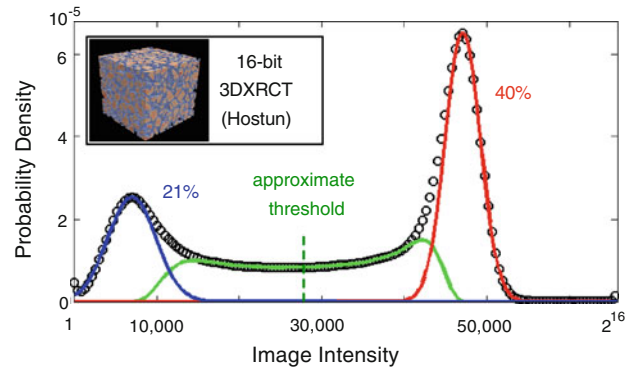


**Fig. 2** Normalized histogram of 3DXRCT intensities of Hostun sand. Data is aggregated over 8 million voxels ( $200^3$  image box). Approximate normal distributions of void (blue) and grain (red) intensities are superposed over experimental data points (black circles). The remaining distribution (green), the difference between the experimental and the two normal distributions, accounts for 39 % of the total volume. For any segmentation algorithm, it is critical to correctly appropriate voxels of the green distribution among the grains and voids (color figure online)

to 39 % of the total. For Caicos ooids (histogram not shown) the area was calculated at 36 % of the total.

As described in Sect. 2.1, the traditional watershed-based methods allocate the voxels of the green distribution using a binary system, classifying each voxel as either grain or void phase. In general, steps can be taken to avoid global volume errors, by choosing the threshold on the basis of sample mass or density. However, little can be done to avoid local artefacts of thresholding, which are enhanced by material granularity.

Figure 3 shows the undesirable artefacts of thresholding an X-ray image of Hostun sand. Specifically, the figure shows that in the regions of grain-to-grain contacts, where X-ray intensities are more saturated due to the mutual proximity of grain surfaces, the grain voxels tend to get over-selected. By extension, assuming the overall density fixed, other grain voxels tend to get under-selected. This inherent threshold bias ultimately hurts the inference of not only grain shape but also contact normals, essential ingredients for studying force transmission and strength in granular media [27]. To our knowledge, only one journal publication [22] has reported

grain fabric, using binarized images of Ottawa sand. Unfortunately, no quantitative details regarding the algorithm were provided, which makes it difficult to relate to the study or judge the accuracy of its results. Another study [2] found a striking statistical bias in grain-to-grain contact normals inferred from 3DXRCT images that were binarised and then separated with a classical watershed algorithm.

The aforementioned bias also negatively affects time-dependent aspects of material structure evolution. For example, to infer grain translations from one (imaged) load state to the next, it becomes necessary to compare the locations of grain centroids, determined from the spatial distribution of grain volumes. Similarly, to infer grain rotations between two (imaged) load states, it becomes necessary to compare principal moments of inertia, which are also determined from the spatial distribution of grain volumes. Rotations, in particular, are extremely sensitive to the surface artefacts identified in Fig. 3. Indeed, the authors are unaware of any study to date that successfully inferred grain rotations using binarized CT images, although advances have been realized recently using other methodologies [2,41].

In the following sections, a new method is presented aiming to address the outlined shortcomings of current segmentation techniques. Before proceeding, it should be noted that it is assumed here that two sets of data are already available: a data file containing a reconstructed greyscale 3DXRCT image, and a binarized data file (0 for void and a non-zero value for a solid phase) where each solid phase voxel is labeled with an integer that denotes a grain number to which it belongs. Individual grains need only be roughly identified.

### 3 Proposed method: the big picture

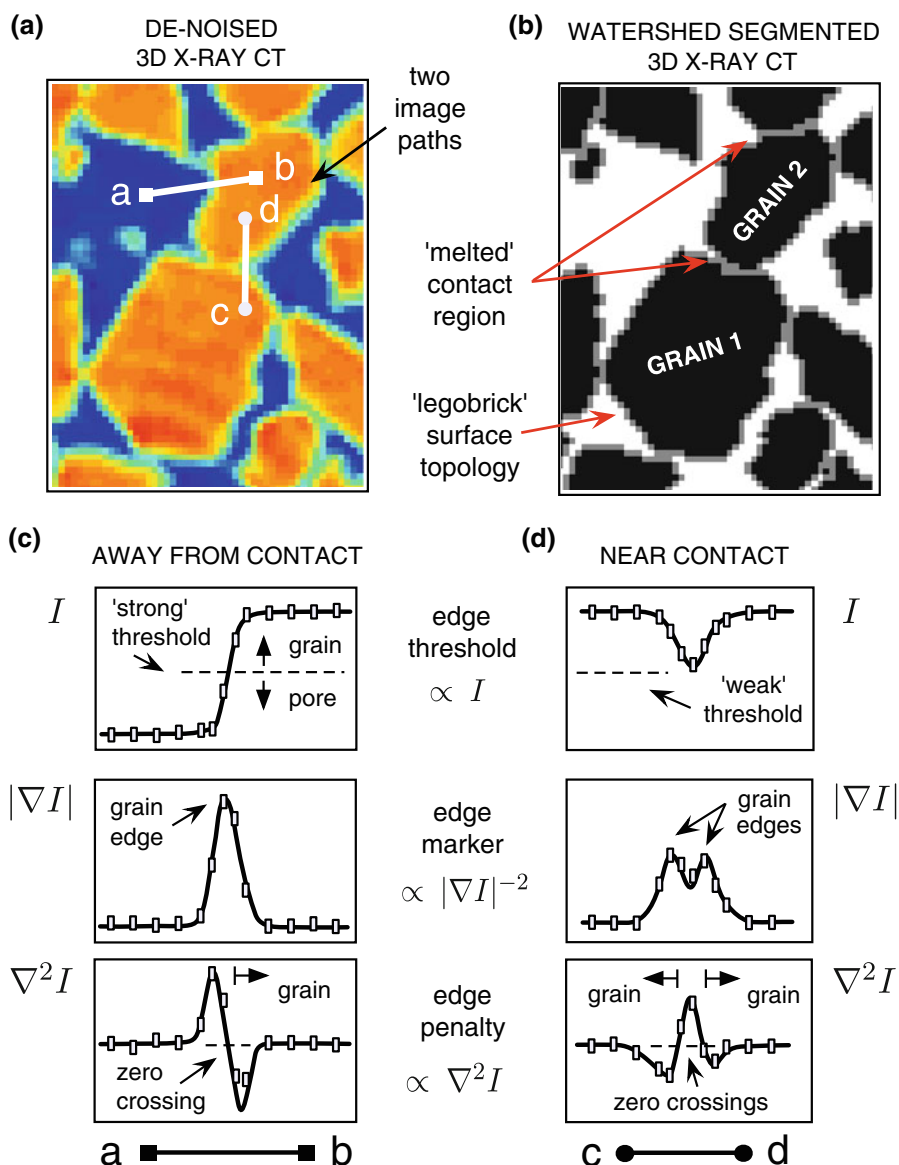
At material scales of the order of particles imaged in this work, approximately 100 micrometers and above, gravity (and capillary) forces dominate [34]. It is at these scales that CT experiments continue to provide unprecedented insight into the material behavior of granular materials (see e.g., [1]). It is also in this regime that grain topology has a great influence on the overall constitutive behavior and strength. Load is carried via inter-particle contacts, the stiffness and strength of which depend on contact shape and orientation per classic Hertz/Mindlin relations (in addition to the inherent material properties). In other words, the parameters controlling the macroscopic response are not only the distribution and orientation of grains, but just as importantly, the interactions between them [29]. At slightly greater scales, highly heterogeneous load chains form in response to external load state (e.g., [28]). When one chain buckles, the system redistributes load, accompanied by grain rearrangement. Capturing these salient features in natural materials has been at the heart of

granular research, in geomechanics and physics departments alike.

As outlined in Sect. 2, the proposed method stands to provide a much-needed direct path to this ultimate goal. Specifically, the proposed method, schematically illustrated in Fig. 4, makes possible an accurate 3D characterization of discrete or granular media from greyscale tomographic images, with sub-voxel resolution and with the ability to resolve grain topology in the near contact regions. The method also returns continuous and differentiable geometry over the entire grain surface, an added benefit of the use of level sets. There are several features of the proposed approach that make the above claims possible. We list them with an intent to provide a bird's eye perspective of the method. An in-depth discussion of the key components, namely the algorithmic details of de-noising and level set algorithms, are given in Sect. 4.

- I *Making use of a full fidelity 3DXRCT image* Whereas watershed-based algorithms make use of binary images ( $2^1$  grey levels) to separate a grain from other grains, the proposed method uses of full fidelity images arising from CT ( $2^{16}$  grey levels). This enables the method to look beyond thresholding to detect grain-to-grain and grain-void boundaries. Together, extrema in the 1st order image gradient and zero-crossings in the 2nd order image gradients provide a strong basis for determining accurate locations of grain surfaces (see Fig. 3).
- II *Reducing image noise* When image gradients (which tend to amplify noise) are used as basis for edge detection, removal of noise is of particular importance. To filter out image noise, while also maintaining sharp edges between individual phases, we make use of advanced non-local de-noising. 3DXRCT histogram is used to provide consistent input parameters across different materials and X-ray attenuation spectra (see Fig. 2 and discussion in Sect. 4.1).
- III *Searching for grain edges via level sets* Edge-based variational LS method is used to isolate objects within an image, using image gradients as input. To this end, a scalar energy functional is defined and minimized, such that in the limit, the zero LS contour is located over the image phase boundaries. Here we also find it necessary to introduce a new penalty procedure to the classic LS in order to resolve issues associated with detection of grain shape near grain-to-grain contact regions. The new penalty procedure ultimately helps recover accurate topology over the entire surface of the grain (see Sect. 4.2 and Fig. 7).
- IV *Improving speed and convergence of level sets* Traditional segmentation methods, i.e., watershed-based methods, provide an excellent basis for distinguishing individual grains in a binary image, albeit with significant

**Fig. 3** Drawbacks of thresholding in granular media. **a** 3DXRCT slice of angular Hostun sand. **b** Undesirable by-products of watershed-based segmentation: melted contacts and stepped legobrick surfaces. **c, d** X-ray intensities plotted for paths in **(a)**. Magnitude of the first image gradient  $|\nabla I|$  and sign changes in the image laplacian  $\nabla^2 I$  are shown to be strong indicators of grain boundaries (solid lines are guides to the eye)



drawbacks as discussed in Sect. 2. Nevertheless, we find that watershed provides a great initial condition for our proposed methodology. Specifically, in search of an energy minimum, LS benefits immensely from a good initial guess. This directly leads to improved stability and faster convergence, as LS does not need to travel far from its starting location in search of grain edges in an image.

Items I–IV describe the main features of the proposed method. Figure 4 provides a schematic representation of a sequence of steps needed to achieve grain characterization from reconstructed CT data. In this work, all steps were also implemented directly in three dimensions. In this way, prob-

lems that may be associated with reconstruction from individual slices do not appear as part of the final solution.

Finally, we note that the proposed method converts digital CT images into a collection of grain avatars, i.e., digitized versions of natural grains. Subsequently, a number of informative operations can be performed. Spatially, one could examine geometric quantities such as grain shape and volume (e.g., Fig. 7), or extract system fabric such the location and orientation of individual contacts (e.g., Fig. 8). In time domain, successive snapshots could be compared (e.g., Fig. 9), such that grain scale processes could be determined as a function of load history. These aspects of analysis will be covered in more quantitative detail in a forthcoming publication.

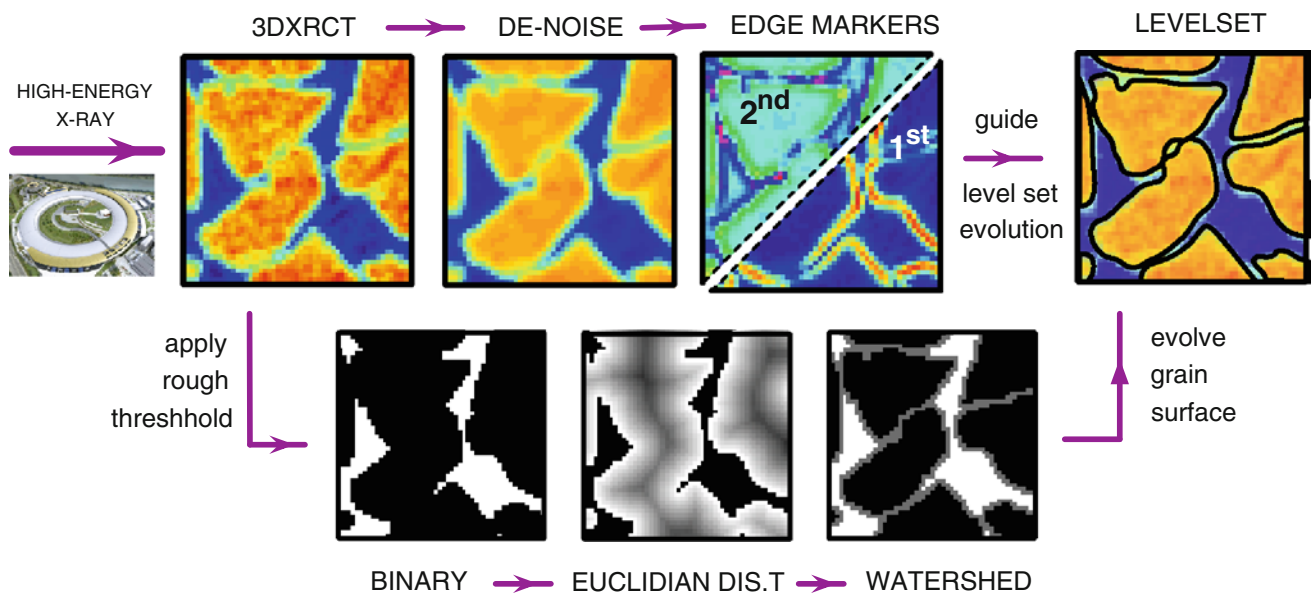


**Fig. 4** Visual schematic of a proposed approach for extracting grains from images of discrete microstructures. The approach, at once, separates the grains from the voids, separates grains from other grains, and provides sub-voxel resolution over the entire grain surface. Validation on 3D natural geomaterials of highly rounded and highly angular shapes

is presented in Sect. 5. [Upper track] Proposed algorithm follows the steps I–IV outlined in Sect. 3. [Lower track] Traditional watershed-based approach provides a starting guess for the spatial locations of individual grains

#### 4 Algorithmic details: image de-noising & level sets

##### 4.1 Removal of noise from CT images

In the presence of noise, detecting phase boundaries within an image can be the extremely difficult [20, 32]. This is because essentially all detection algorithms consider image gradients, using either maxima in the 1st order gradients or so-called zero crossings in the 2nd order gradients as boundary indicators [23] (see Fig. 3c,d). Image gradients, however, tend to amplify (rather than reduce) noise in images. As a result, even a visually recognizable feature in an image can be entirely missed from the gradients. Reduction of noise is a necessary first step in boundary detection.

A good de-noising algorithm should be able to clean up the local intensity variations and preserve image sharpness in areas of importance, e.g., near phase edges or grain-to-grain contacts, all without an a priori knowledge of what a noise-free image looks like. To accomplish this, *all* de-noising approaches rely on one underlying idea—averaging—but differ in terms of what to average, as well as in their success at doing so. For completeness, we first review the two most popular noise reduction algorithms (Gauss and Median filters), before focusing on a more successful and recently published algorithm (Non-Local Means filter). The latter is used as part of the proposed methodology in this paper.

Gauss filter (GF), shown in Eq. (4.1), is amongst the simplest and the most commonly applied de-noising filters. Local

in nature, it is based on an implicit assumption that pixels (or voxels in 3D) which appear near to each other in an image are also most likely to be similar to each other. As such, GF performs a weighted average over a small window  $I(\mathbf{x} + \mathbf{t})$  centered at  $\mathbf{x}$  in the raw image domain and assigns the computed scalar value to an output image  $I^{GF}(\mathbf{x})$ , as shown in Eq. (4.1). In more formal terms, GF returns a weighted average over an image area  $\mathbf{x} + \mathbf{t}$  using a discrete Gaussian kernel  $G_\rho(\mathbf{t})$ , whose weights decay exponentially as function of a distance  $\mathbf{t}$  from the location  $\mathbf{x}$  of a source pixel.  $\rho$  is a standard deviation of the Gaussian distribution. A constant  $C$  assures that over a finite domain, the sum of all weights  $G_\rho(\mathbf{t})$  is unity. Filtering using GF can be performed very quickly using standard convolution methods, since the Gauss kernel is separable into its uni-directional components., e.g., in 2D one can first apply the kernel in the x-direction, followed by the y-direction. GF minimizes local image fluctuations well, but is diffusive and leads to blurring of edges (loss of sharpness).

$$I^{GF}(\mathbf{x}) = G_\rho(\mathbf{t}) I(\mathbf{x} + \mathbf{t})$$

$$\text{where } G_\rho(\mathbf{t}) = \frac{1}{C} \exp\left[-\frac{\mathbf{t} \cdot \mathbf{t}}{2\rho^2}\right] \quad (4.1)$$

Median filter (MF), shown in Eq. (4.2), is another popular de-noising technique. It is identical to GF in all ways except one: instead of performing a weighted average over a local image neighborhood  $\mathbf{x} + \mathbf{t}$ , MF extracts a median pixel value

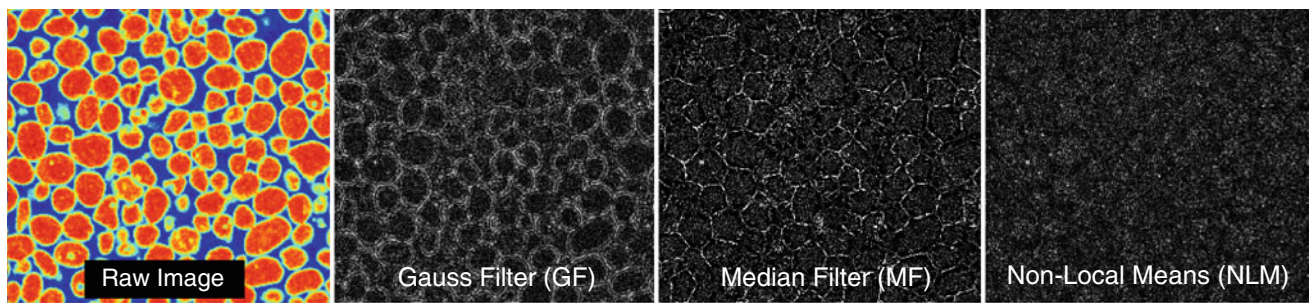


**Fig. 5** Comparison of noise-removal techniques for a slice of rounded sand, Caicos ooids. (Far left) Raw image slice from reconstructed 3DXRCT. (All other) Noise pattern subtracted from (a), with *light color* indicating the greatest difference. That grain outlines can be visually

identified from GF and MF noise patterns indicates that these filters remove too much important detail from phase/grain boundaries. Note: prior to comparison, all techniques were adjusted to provide a similar level of de-noising (see text for details)

from this neighborhood and assigns a scalar value to an output image  $I^{MF}(\mathbf{x})$ . To this end, all pixels in a neighborhood are first sorted based on their numerical value, and the pixel being considered is subsequently replaced with the middle value of the sorted list, i.e., the median. As intuitively expected, MF is very successful in removing local outliers. But again, this is accomplished at the expense of edge sharpness, particularly in proximity to grain-to-grain contacts.

$$I^{MF}(\mathbf{x}) = \text{median} \{ I(\mathbf{x} + \mathbf{t}) \} \tag{4.2}$$

Significant improvements over both GF and MF can be realized by identifying neighborhoods across an entire image that are of ‘similar context’ and averaging based on the degree of similarity between these windows, regardless of their proximity to the source. These techniques are by nature non-local, and increasingly sophisticated variants have been developed over the years. We focus on a particularly successful and recently proposed de-noising algorithm: Non-Local Means (NLM) [9, 10]. We choose this particular algorithm because it is extremely intuitive and relatively simple to implement.

The underlying steps of NLM as shown in Eq. (4.3) are the following. Compare a source image window  $I(\mathbf{x} + \mathbf{t})$  with all other windows across the image  $I$ , namely  $I(\mathbf{y} + \mathbf{t})$ . For each window of comparison, calculate a scalar weight  $w(\mathbf{x}, \mathbf{y})$  dependent on the Euclidian distance  $\|I(\mathbf{x} + \mathbf{t}) - I(\mathbf{y} + \mathbf{t})\|$ . Give less importance to pixels away from the window centers via discrete Gaussian kernel  $G_\rho(\mathbf{t})$  (identical to  $G_\rho(\mathbf{t})$  in (4.1)) and scale the Euclidian distance by a value of noise variance  $h$ . Once the weights are collected, perform a weighted average over all window centers  $I(\mathbf{y})$  and assign the result to the source pixel  $I^{NLM}(\mathbf{x})$ , i.e., the pixel in the center of the source window. A constant  $\mathcal{C}(\mathbf{x})$  assures that the sum of all weights  $w(\mathbf{x}, \mathbf{y})$  is unity. In this way, averaging is no longer based on proximity or distance from the source pixel (i.e., local), but it is rather a function of the context in which the pixels appear (i.e., non-local).

$$I^{NLM}(\mathbf{x}) = \frac{1}{\mathcal{C}(\mathbf{x})} \int_I w(\mathbf{x}, \mathbf{y}) I(\mathbf{y}) d\mathbf{y}$$

where  $w(\mathbf{x}, \mathbf{y})$

$$= \exp \left[ -\frac{G_\rho(\mathbf{t}) \|I(\mathbf{x} + \mathbf{t}) - I(\mathbf{y} + \mathbf{t})\|}{2h^2} \right] \tag{4.3}$$

In comparison to GF, NLM contains two additional parameters. The first is the image noise variance  $h$ , a physical parameter that can be conveniently estimated from the image histogram. In this work, the variance is taken as an average variance of the pore and grain X-ray intensities (e.g., variance of blue and red Gauss distributions in Fig. 2). The other additional parameter is the size of a non-local search window. In practice, it is too expensive computationally to compare a source window  $I(\mathbf{x} + \mathbf{t})$  to all other image windows of the same size. Instead, a comparison is typically restricted to a vicinity of the source pixel (see [9, 10] for details), without adverse effects on the filter performance. In this work, the search is restricted to a radius of 15 voxels from the source.

In Fig. 5, we compare NLM with GF and MF because literature on edge detection almost exclusively uses these two filters as a pre-processing step. To provide a roughly equal basis for comparison, input parameters for GF and NLM filters were adjusted so as to provide a visually similar degree of de-noising to MF, whose local window  $I(\mathbf{x} + \mathbf{t})$  was fixed to  $3 \times 3$  pixels. This led to a GF filter with standard deviation  $\rho$  of 0.75 pixel lengths applied over a discrete  $7 \times 7$  Gaussian kernel. For NLM a source window size of  $5 \times 5$  with a comparison search restricted to a neighborhood of  $31 \times 31$  pixels centered at the source pixel was fixed, while noise variance was adjusted until a degree of smoothing visually similar to GF and MF was obtained, leading to  $h = 1500$  (out of  $2^{16}$  or 65,536 greyscale values), about 50% lower than estimated based on the 3DXRCT image histogram.

Based on the visual indicators in Fig. 5, NLM is shown to reduce image noise extremely well, particularly for discrete media where it is able to reduce noise from within phases

while preserving sharpness both at grain-void boundaries and grain-to-grain contacts. A more quantitative series of comparisons of NLM with other filters can be found in [9]. Within our proposed methodology schematically described in Fig. 4, NLM is also the most computationally consuming step. However, we found it to be indispensable, as evident from the results in Sect. 5, Fig. 7.

For completeness, we note several publications which improve upon the basic premise of NLM (not implemented as part of this work). These include improvements in weighing parameters [13], iterative filtering [21], and overall efficiency [8, 14].

## 4.2 Grain surface detection using active level set contours

### 4.2.1 Detecting isolated grains

Since their introduction a little over two decades ago [31], level sets (LS) have been extremely useful as a computational tool in problems involving interfaces. The primary draw of LS is that they enable motion of very complex interfaces and shapes to be computed on a fixed Eulerian grid (rather than via Lagrangian parametric space), with the direction and magnitude of the interface motion arbitrarily dependent on the interface geometry. LS operate in a space that is a single dimension higher than the space where an interface resides, as schematically illustrated in Fig. 6. In this way, an interface can be represented as the (zero) level contour  $C$  of some imbedding function  $\phi : \Omega \rightarrow \mathbb{R}$ , such that  $C = \{x \in \Omega \mid \phi(x) = 0\}$ , where  $\Omega$  is a plane or a volume [15, 30]. For example, to describe a three-dimensional shape such as

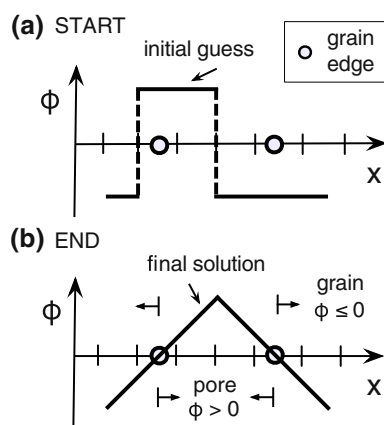


**Fig. 6** Schematic of a 1D level set problem geometry. Boundaries to be detected are shown as *open circles* in 1D. **a** An approximate (binary) initial guess of a level set (LS) function  $\phi(x)$  at  $t = 0$ . This could be an output of a traditional segmentation technique, e.g., watershed. **b** Final solution, ultimately taking the form of a continuous distance function. Note that  $\phi(x)$  is always one dimension higher than the problem domain. Also, grain boundaries  $\phi(x) = 0$  can be arbitrarily located on a computational grid

a sand grain, one would need a four-dimensional function (one scalar value for every location  $x, y, z$  on a fixed Eulerian grid). Every zero crossing of that function would represent a point on the surface of the grain, while a full zero level contour would describe the entire grain surface.

In the context of this work, we utilize edge-based variational LS [12, 24] in order to locate a grain surface in a reconstructed 3DXRCT image. In a variational framework, an object (in this case grain) is segmented from an image by locally minimizing an appropriate energy functional. To this end, LS function of same size as the image domain is created, and its zero level LS contour is subsequently evolved until the scalar energy functional of LS function is minimized. The functional is at a minimum when the zero level contour is optimally located over large gradients of the XRCT image. The specific details of how this is accomplished are described next.

For our contribution, we adopt a particular variational framework [25, 26], termed distance regularized level set evolution (DRLSE), because of its two favorable traits: (1) An initial LS function, i.e.,  $\phi(x, y, z, t = 0)$ , can be a binary function, which allows a binarized image to serve as a starting guess, and (2) No LS re-initialization is needed during its evolution, which simplifies numerical implementation tremendously. Equation (4.4) shows the energy functional  $\mathcal{E}$  of DRLSE,

$$\mathcal{E}(\phi, I) = \mu \mathcal{R}(\phi) + \lambda \mathcal{L}(\phi, I) + \alpha \mathcal{A}(\phi, I) \quad (4.4)$$

where the three terms on the right-hand side of Eq. (4.4) work in tandem to identify the most likely location of object boundaries within an image. These contain three fixed constants, namely  $\mu$ ,  $\lambda$ , and  $\alpha$ . Minimization of the DRLSE energy functional in (4.4), i.e., the evolution of the contour in the direction of the negative energy gradient, leads to the following expression [25]:

$$\begin{aligned} \frac{\partial \phi(\mathbf{x})}{\partial t} &= \mu R(\phi) + \lambda L(\phi, I) + \alpha A(\phi, I) \\ R(\phi) &= \nabla \cdot (d(\phi) \nabla \phi) \\ L(\phi, I) &= \delta(\phi) \nabla \cdot \left( g(I) \frac{\nabla \phi}{\|\nabla \phi\|} \right) \\ A(\phi, I) &= \delta(\phi) g(I) \\ \delta(\phi) &= \begin{cases} \frac{1}{2a} \left( 1 + \cos \frac{\pi \phi}{a} \right) & \text{if } \text{abs}(\phi) \leq a \\ 0 & \text{if } \text{abs}(\phi) > a \end{cases} \\ d(\phi) &= \begin{cases} \frac{1}{2\pi} \frac{\sin(2\pi \|\nabla \phi\|)}{\|\nabla \phi\|} & \text{if } \|\nabla \phi\| < 1 \\ \frac{\|\nabla \phi\| - 1}{\|\nabla \phi\|} & \text{if } \|\nabla \phi\| \geq 1 \end{cases} \\ g(I) &= \frac{1}{1 + \|\nabla I\|^2} \end{aligned} \quad (4.5)$$

The first term of the right side of Eq. (4.5),  $R(\phi)$ , is a stabilizing term which helps maintain a smooth (distance) profile of the LS function during its evolution. At all times,  $R(\phi)$  works to keep the signed distance profile of LS, or rather the magnitude of its gradient equal to unity near its zero-level contour. This term also represents a fundamental contribution of DRLSE over classic edge-based variational approaches which require periodic re-initialization. The second and third terms, namely  $L(\phi, I)$  and  $A(\phi, I)$  are so-called external energy terms, directly incorporating image information  $I$ . Specifically,  $L(\phi, I)$  is a contour integral of the LS function.  $L(\phi, I)$  is minimized when the zero LS contour is located over the boundaries of an object within an image, as indicated by an edge marker  $g(I) \propto \|\nabla I\|^{-2}$  that heavily favors locations of large image gradients. The third term,  $A(\phi, I)$ , is a ‘balloon force’ or a weighted area integral. This term speeds the motion of the zero LS contour, scaled by the edge marker  $g(I)$ . While not strictly necessary,  $A(\phi, I)$  helps move the contour outward (or inward depending on the sign of  $\alpha$ ) in order to improve time to convergence. Evolutions of both  $L(\phi, I)$  and  $A(\phi, I)$  are restricted by a smooth Dirac delta function  $\delta(\phi)$  to a narrow band of  $\phi \leq a$ , with  $a$  equal to  $3/2$ .

The stabilizing term  $R(\phi)$  simplifies numerical implementation of DRLSE tremendously. It provides diffusivity to (4.5), enabling gradients to be expressed via a central finite differences as well as allowing explicit time integration. The initial condition  $\phi(t = 0)$  is supplied by the scaled binarized image, with its zeros set to  $a + 1/2 = 2$  and ones set to  $a - 1/2 = -2$ . This scaling is needed because in the LS formulation, grain boundary is defined by a zero level contour, while in a binary image, that contour is  $1/2$ . At domain edges, Neumann boundary conditions are imposed by setting the gradient of  $\phi$  null. While the applications of DRLSE have thus far been restricted to 2D images (we are not aware of 3D implementations in literature), we find that extending it to 3D images such as 3DXRCT presents no additional complications.

Thus far, the discussion in this section has implicitly assumed that objects (or grains) to be segmented are isolated from one another. When in contact, basic DRLSE is not sufficient and enhancements of Eq. (4.5) are necessary. This is the subject of the next section.

### 4.2.2 Detecting contacting grains

In images of discrete media, where individual objects (e.g., grains) may be in contact, or more generally where  $\|\nabla I\|$  may not have a single distinct maximum (e.g., see Fig. 3d), DRLSE tends to ‘leak’. In other words, in search for an edge without a single, clear gradient maximum, zero LS contour may not slow down sufficiently, overshoot the boundary of

the target object, leak into another contacting object, and never recover. We found this to be a real, and clearly undesirable problem. As a remedy, we introduce two modification to classic DRLSE:

- I *Level set competition* Introduce two LS functions, penalizing any overlap between the two [19,43]. The first,  $\phi_1$ , is assigned to a grain under consideration, and the second,  $\phi_2$  is assigned to all other grains in a computational window. Any attempt by  $\phi_1$  to ‘leak’ into any other grain will be met with resistance from  $\phi_2$  when in contact. In this way, a single grain can always be segmented with no more than two LS functions, regardless of the number of other contacting grains.
- II *Zero-crossing penalty* Some edges, particularly those near grain-to-grain contact, may not have a strong gradient maximum. Here, zero-crossings of the 2nd order gradient, characterized by image laplacian  $\nabla^2 I$ , are excellent predictors of edges (see Fig. 3c,d). In practice, searching for the exact locations of zero-crossings is cumbersome and tends to yield too many false positives. Instead, we note that  $\nabla^2 I$  is positive in the void regions near contact (grains have a greater X-ray attenuation than the surrounding voids). We incorporate this in the form of a penalty term that progressively slows down or outright stops the evolution of LS, depending on the magnitude of  $\nabla^2 I > 0$ .

Together, modifications I and II yield a variational LS in (4.6) that is better tailored to images of discrete media:

$$\frac{\partial \phi_i(\mathbf{x})}{\partial t} = \underbrace{\mu R(\phi_i) + \lambda L(\phi_i, I) + \alpha A(\phi_i, I)}_{\text{classic DRLSE, (4.5)}} + \underbrace{\beta P(\phi_i, \phi_j, I)}_{\text{modifications I and II}} \quad \text{for } i, j = 1, 2, \quad i \neq j$$

$$P(\phi_i, \phi_j, I) = \delta(\phi_i) (F(I) + H(-\phi_j))$$

$$H(\phi) = \begin{cases} \frac{1}{2a} \left( 1 + \frac{\phi}{a} + \frac{1}{\pi} \sin \frac{\pi \phi}{a} \right) & \text{if } \text{abs}(\phi) \leq a \\ 1 & \text{if } \phi > a \\ 0 & \text{if } \phi < -a \end{cases} \quad (4.6)$$

$$F(I) = \begin{cases} n \nabla^2 I & \text{if } \nabla^2 I \geq 0 \\ 0 & \text{if } \nabla^2 I < 0 \end{cases}$$

Note that the sole difference between Eqs. (4.5) and (4.6) is the presence of two competing LS functions,  $\phi_1$  and  $\phi_2$ , as well as an additional term  $P(\phi_i, \phi_j, I)$  which specifies the interactions between  $\phi_1$  and  $\phi_2$ ;  $\beta$  is a constant. Only the terms not previously defined are expanded in Eq. (4.6).

The additional term  $P(\phi_i, \phi_j, I)$  incorporates modifications I and II. Specifically, interpenetration between LS functions is penalized via a smooth Heaviside function  $H(\phi)$ . Similarly, the motion of both LS functions into regions where

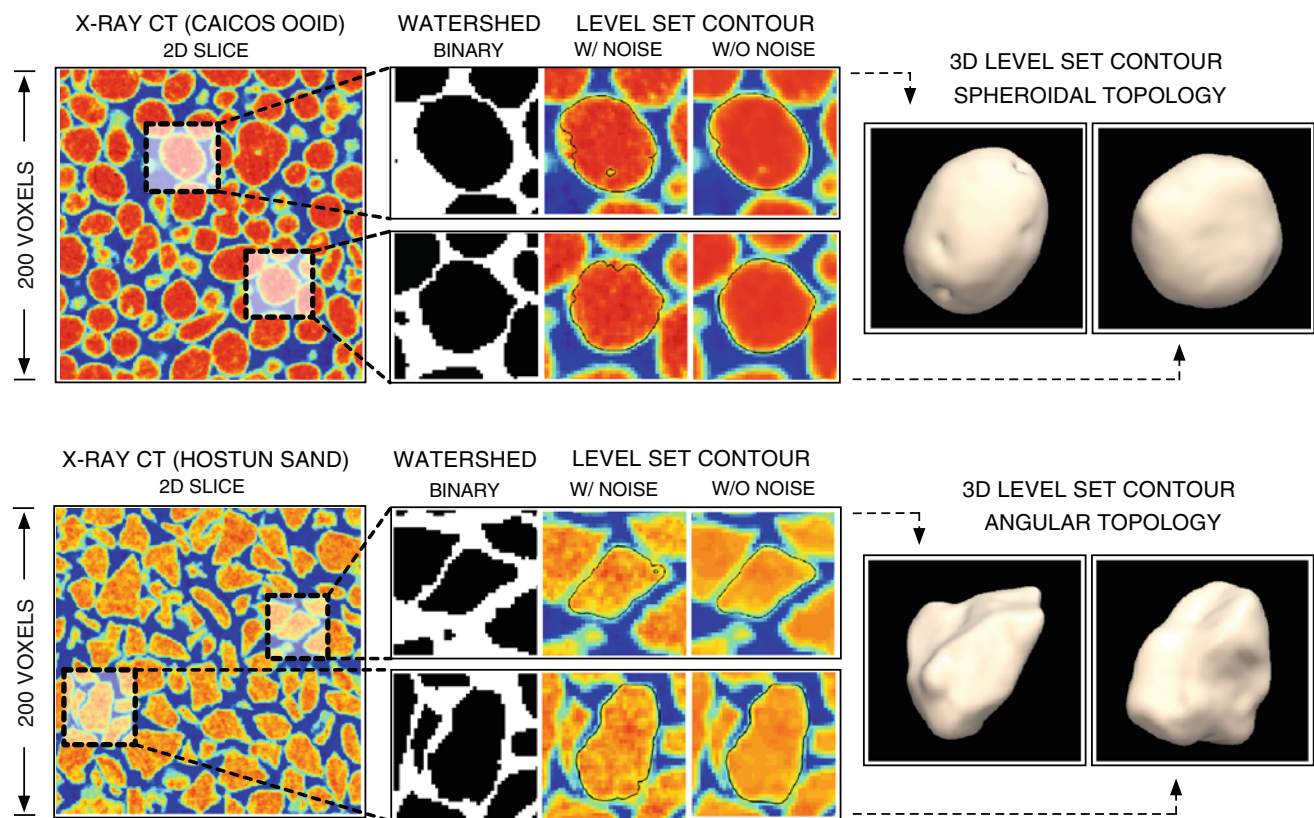


**Fig. 7** Characterization of rounded Caicos ooids (*top*) and angular Hostun sand (*bottom*). (*Left*) A slice through a 16-bit 3DXRCT volume of  $200^3$  voxels (approximately  $1\text{mm}^3$ ). Representative grains varying from  $19^3$ – $25^3$  voxels in volume were chosen at random from each sample and segmented directly in 3D using the techniques described in this

paper. (*Middle*) Grains shown at higher magnification. The proposed technique (LS with prior image de-noising) captures the grain surfaces faithfully and with consistency. (*Right*) Grains rendered in Paraview (via a 3D Contour filter) without any topological modifications or enhancements

image laplacian  $\nabla^2 I > 0$  is penalized via  $F(I)$ . The latter primarily affects areas in the vicinity of grain-to-grain contacts, where image laplacian is strongly positive. Parameter  $n$ , equal to the mean of the positive values of  $\nabla^2 I$ , normalizes the magnitude of the image laplacian.

In terms of implementation,  $\phi_1(t = 0)$  is first initialized as a binary function of the grain to be segmented.  $\phi_2(t = 0)$  is initialized as a binary function of all other grains in the computational domain.  $\phi_1$  and  $\phi_2$  are further modified by adding an extra layer to solid voxels, and linearly mapping the binary  $[0, 1]$  to a more appropriate  $[2, -2]$  domain, as discussed in the previous section. Equation (4.6) is implemented as before, via standard 2nd order central finite differences, with Neumann boundary conditions enforced at all domain limits. There are a total of five constants used for all figures generated in this work: time increment  $\Delta t = 1$  with  $\mu = 0.001$ ,  $\lambda = 2$ ,  $\alpha = -3$ , and  $\beta = 2$ . A high value of  $\beta$  leads to faster convergence (on average, around 200–500 time steps), but also biases the results toward lower than actual grain volumes. Evolution of LS is terminated when either the zero crossing points stop varying for consecutive iterations or exceed a prescribed maximum number of itera-

tions [25]. Here we used a latter termination criterion, capped at 300 iterations. The results using 3DXRCT images of natural geomaterials are presented next.

## 5 Results on natural granular media

In this section, we use the proposed methodology to characterize two morphologically different geomaterials. Hostun sand, named after its town of origin in the south-east of France, is a plain sand. Its grains result from a gradual breakdown of rock due to weathering, leading to angular or sub-angular grain shapes. Primarily composed of silica, Hostun sand is a reference material in soil mechanics - its mechanical properties have been studied for decades (e.g., [17,18]). On the other hand, Caicos ooids originate in the warm, tropical waters of the Bahamas island chain. While still a sand (based on their physical size), ooids do not begin their life as rock. Rather, they grow from seeds or nuclei, which can themselves be fragments of quartz or shell. They accumulate layers in time, a result of chemical precipitation

from a saturated aqueous environment. This mechanism of formation leads to unusually smooth and rounded grains.

Both sand types were imaged non-destructively during a series of triaxial load states. The samples were first confined isotropically, followed by a series of axial strain-controlled load increments. At the conclusion of each load increment, sample is rotated and as series of XRCT images was collected (see [3] for details). Overall, samples contained enough grains to allow experiments to reproduce classic failure mechanism of these materials, i.e., shear bands for the dense granular packings. In terms of resolution, each grain was composed of roughly  $15^3 - 25^3$  voxels, a volumetric equivalent of a sphere of 9–16 voxels in radius. Following the experiments, individual CT radiographs were reconstructed into 3DXRCT greyscale images. Thereafter, density-based thresholding followed by a traditional watershed-based segmentation was performed. This sequence of steps followed the state of the art in characterization of imaged granular media, as schematically shown in Fig. 1. Data arising from these steps provide a starting point for our proposed algorithm, as outlined in Sect. 2.1 and schematically shown in Fig. 4.

Figures 7 through 9 showcase a range of properties that can be extracted using our proposed algorithm—including the topology of individual grains, interactions amongst a group of grains, and incremental grain kinematics over a series of images corresponding to different material states. In all figures, grains of Caicos and Hostun were extracted using an identical set of algorithmic parameters, as outlined in Sect. 4.2. To plot each grain,<sup>2</sup> its level set function was exported directly to Paraview and its zero contour rendered using a built-in contour filter, without any topological modifications or enhancements. Based on Figs. 7 through 9 we find the presented technique to be highly effective in characterizing granular systems whose discrete nature makes them poor candidates for classic LS segmentation techniques.

Perhaps the most remarkable part of the results is that the grain surfaces in Fig. 7 correctly reflect the expected morphologies of two very different geomaterials. Specifically, Caicos ooids appear well rounded, while Hostun sand shows a high degree of angularity, an expected outcome based on the materials' geologic mechanisms of formation. The center images in Fig. 7 also illustrate a key sequence of steps needed to obtain final 3D grain shapes. This includes a rough initial guess, as provided by the watershed-based algorithm, and improvements in calculated image gradients, as enabled by the non-local NLM de-noising filter.

<sup>2</sup> Recall that our proposed technique ultimately yields one level set function for each grain, i.e., a scalar value for each node on a regular Eulerian grid. A zero contour of this function describes the surface of a chosen grain.

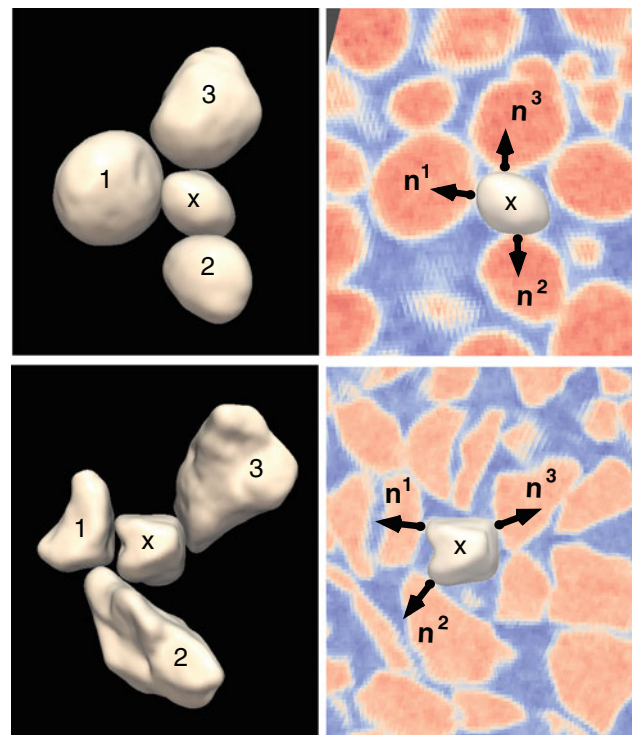


**Fig. 8** Multiple grains of Caicos ooids (*top*) and Hostun sand (*bottom*) in contact. (*Left*) Grains rendered in Paraview (via a 3D contour filter), without any topological modifications or enhancements. X marks a central grain and numbers 1–3 mark the three grains in contact with the central grain. (*Right*) Contact orientations projected on a plane common to the three contact points. On the same plane, 3DXRCT image projection is shown

That surface topology of grains in Fig. 7 do not appear to be significantly affected by their surroundings, especially by several other grains which are in contact with them (not all visible from a 2D slice), suggests that more reliable measurements of contact properties should be on the horizon. This point is schematically shown in Fig. 8 where three contacting grains around a central grain are rendered in two different flavors: (at left) with grains isolated from their surroundings, and (at right) with a central grain over a projected 3DXRCT image in a plane containing the three points of contact. Projected contact orientations are visually estimated.

Figure 9 provides a visual indicator of the resolution available for inference of grain kinematics. The inset indicates the size of the tested granular sample and the boundary conditions applied to it. The ultimate failure plane, or shear band, is also shown in relation to the global axes. Here, a Caicos grain originating from a region that will ultimately be a part of a failure band is followed during two (macroscopically) equal strain increments: the first, imaged at the start of testing (small strain inside the shear band) and the second, during the approach to critical state (large strain inside the shear band). As Fig. 9 shows, both increments appear with enough resolution so as to visually provide high-fidelity grain kinematics.

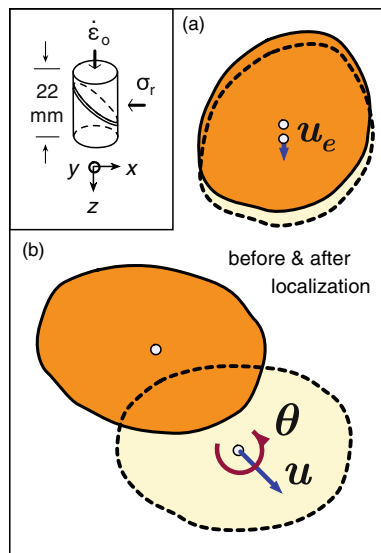


**Fig. 9** Grain kinematics inside a shear band during two equal macroscopic strain increments. (Inset) Macroscopic boundary conditions, with the shear (localization) band shown in relation to the global axis. **a** and **b** Grain contours of a Caicos ooid, in a plane of inset global axis. Grain resolution afforded by the proposed methodology allows for direct assessment of grain-scale kinematics. Note: differences between contours in **(a)** and **(b)** are due to significant out-of-plane grain rotation between the two load stations

matics, both in terms of the translations and rotations. To give a sense of magnitude, grain motion during the early load step in Fig. 9a corresponds to roughly 1 voxel length of vertical (z-direction) displacement.

That the presented method is able to successfully characterize natural materials with sub-image resolution, despite the inherent noise in elemental grain composition and XRCT image capture, suggests significant promise. Planned future studies will provide more focus to statistical aspects of the granular material response.

## 6 Summary

We have presented a level set-based methodology for enhanced quantitative characterization of particle morphology. The new technique affords *avant-garde* imaging techniques, epitomized by X-ray computed tomography, the real possibility of accurately quantifying kinematics and spatial interactions amongst grains as a function of macroscopic processes, e.g., deformation under load. This new technique makes full use of grayscale image data arising from CT and then filters it to furnish precise edge markers via the first and second gradients of X-ray attenuation. Using these markers and current segmentation techniques (e.g., watershed) as initial conditions, level sets are allowed to evolve until the boundary of particles is identified and, consequently,

mathematically characterized. The very challenging region of grain-to-grain contact is accurately resolved by using two competing level set functions, one belonging to the source grain and the other belonging to other grains in the computational field of view. In this way, the proposed methodology ultimately enables a quantitative description of particle shape, particle kinematics, and characteristics of neighboring contacts. This information is crucial to quantify the micro mechanical essence of granular matter: fabric, kinematics, and contact forces [11]. Armed with this information, future models can more accurately describe the micro mechanics of granular materials (e.g., using discrete methods [6]) based directly on in situ experiments, and ultimately lead to ‘tomography-to-simulation’ paradigms that can unify micro and macro mechanical processes in granular materials [7].

**Acknowledgments** This work is supported in part by W.M. Keck Institute for Space Studies. This support is gratefully acknowledged.

## References

- Alshibli, K.A., Reed, A.H. (eds.): *Advances in Computed Tomography for Geomaterials*. Wiley, New Orleans, USA (2010). doi:[10.1002/9781118557723](https://doi.org/10.1002/9781118557723)
- Andò, E., Hall, S., Desrues, J., Viggiani, G., Bésuelle, P.: Experimental micromechanics: grain-scale observation of sand deformation. *Géotech. Lett.* (2012a). Accepted
- Andò, E., Hall, S., Viggiani, G., Desrues, J., Bésuelle, P.: Grain-scale experimental investigation of localised deformation in sand: a discrete particle tracking approach. *Acta Geotech.* **7**, 1–13 (2012b). doi:[10.1007/s11440-011-0151-6](https://doi.org/10.1007/s11440-011-0151-6)
- Andrade, J.E., Tu, X.: Multiscale framework for behavior prediction in granular media. *Mech. Mater.* **41**(6), 652–669 (2009)
- Andrade, J.E., Avila, C.F., Hall, S.A., Lenoir, N., Viggiani, G.: Multiscale modeling and characterization of granular matter: from grain kinematics to continuum mechanics. *J. Mech. Phys. Solids* **59**, 237–250 (2010)
- Andrade, J.E., Lim, K.-W., Avila, C.F., Vlahinić, I.: Granular element method for computational particle mechanics. *Comput. Methods Appl. Mech. Eng.* **241**, 262–274 (2012). doi:[10.1016/j.cma.2012.06.012](https://doi.org/10.1016/j.cma.2012.06.012)
- Andrade, J.E., Vlahinić, I., Lim, K.-W., Jerves, A.: Multiscale tomography-to-simulation framework for granular matter: the road ahead. *Géotech. Lett.* **2**, 135–139 (2012b). doi:[10.1680/geolett.12.00023](https://doi.org/10.1680/geolett.12.00023)
- Brox, T., Kleinschmidt, O., Cremers, D.: Efficient nonlocal means for denoising of textural patterns. *IEEE Trans. Image Process* **17**, 1083–1092 (2008)
- Buades, A., Coll, B., Morel, J.-M.: A review of image denoising methods, with a new one. *Multiscale Model. Simul.* **4**, 490–530 (2005). doi:[10.1007/s11263-007-0052-1](https://doi.org/10.1007/s11263-007-0052-1)
- Buades, A., Coll, B., Morel, J.-M.: Nonlocal image and movie denoising. *Int. J. Comput. Vis.* **76**, 123–139 (2008). doi:[10.1007/s11263-007-0052-1](https://doi.org/10.1007/s11263-007-0052-1)
- Calvetti, F., Combe, G., Lanier, J.: Experimental micromechanical analysis of 2d granular material: relation between structure evolution and loading path. *Mech. Cohesive-Frict. Mater.* **2**, 121–163 (1997)

12. Caselles, V., Catté, F., Coll, T., Dibos, F.: A geometric model for active contours in image processing. *Numer. Math.* **66**, 1–31 (1993). doi:[10.1007/bf01385685](https://doi.org/10.1007/bf01385685)
13. Chatterjee, P., Milanfar, P.: A generalization of non-local means via kernel regression. In: *Proceedings of Computational Imaging (2008)*
14. Coupe, P., Yger, P., Prima, S., Hellier, P., Kervrann, C., Barillot, C.: An optimized blockwise nonlocal means denoising filter for 3-d magnetic resonance images. *IEEE Trans. Med. Imaging* **27**, 421–441 (2008). doi:[10.1109/tmi.2007.906087](https://doi.org/10.1109/tmi.2007.906087)
15. Cremers, D., Rousson, M., Deriche, R.: A review of statistical approaches to level set segmentation: integrating color, texture, motion, and shape. *Int. J. Comput. Vis.* **72**, 195–215 (2007). doi:[10.1007/s11263-006-8711-1](https://doi.org/10.1007/s11263-006-8711-1)
16. Desrues, J., Viggiani, G., Bésuelle, P. (eds.): *Advances in X-ray Tomography for Geomaterials*, 1st edition. Wiley-ISTE, 2006. doi:[10.1002/9780470612187](https://doi.org/10.1002/9780470612187)
17. Desrues, J., Viggiani, G.: Strain localization in sand: an overview of the experimental results obtained in grenoble using stereophotogrammetry. *Int. J. Numer. Anal. Methods Geomech.* **28**, 279–321 (2004)
18. Flavigny, E., Desrues, J., Palayer, B.: Note technique le sable d'hostun rf. *Rev. Franc. Géotech.* **53**(53), 67–70 (1990)
19. Gao, H., Chae, O.: Individual tooth segmentation from ct images using level set method with shape and intensity prior. *Pattern Recognit.* **43**, 2406–2417 (2010). doi:[10.1016/j.patcog.2010.01.010](https://doi.org/10.1016/j.patcog.2010.01.010)
20. Gonzalez, R.C., Woods, R.E.: *Digital Image Processing*, 3rd edn. Prentice Hall, Upper Saddle River (2008)
21. Goossens, B., Luong, H., Pizurica, A., Philips, W.: An improved non-local denoising algorithm. In: *Proceedings International Workshop on Local and Non-Local Approximation in Image Processing (LNLA)* (2008)
22. Hasan, A., Alshibli, K.: Three dimensional fabric evolution of sheared sand. *Granul. Matter* **14**, 469–482 (2012). doi:[10.1007/s10035-012-0353-0](https://doi.org/10.1007/s10035-012-0353-0)
23. Hladuvka, J., König, A., Gröller, E.: Exploiting eigenvalues of the hessian matrix for volume decimation. In: *9th International Conference on Computer Graphics, Visualization, and Computer Vision (WSCG)*, pp. 124–129 (2001)
24. Kichenassamy, S., Kumar, A., Olver, P., Tannenbaum, A., Yezzi, A.: Conformal curvature flows: from phase transitions to active vision. *Arch. Ration. Mech. Anal.* **134**, 275–301 (1996)
25. Li, C., Xu, C., Gui, C., Fox, M.D.: Distance regularized level set evolution and its application to image segmentation. In *Proceedings of IEEE, Image Processing*, pp. 3243–3254 (2010)
26. Li, C., Xu, C., Gui, C., Fox, M.D.: Level set evolution without re-initialization: a new variational formulation. In: *Proceedings of IEEE, Computer Vision and Pattern Recognition*, pp. 430–436 (2005)
27. Li, X., Dafalias, Y.: Anisotropic critical state theory: role of fabric. *J. Eng. Mech.* **138**, 263–275 (2012). doi:[10.1061/\(ASCE\)EM.1943-7889.0000324](https://doi.org/10.1061/(ASCE)EM.1943-7889.0000324)
28. Majmudar, T.S., Behringer, R.P.: Contact force measurements and stress-induced anisotropy in granular materials. *Nature* **435**, 1079–1082 (2005). doi:[10.1038/nature03805](https://doi.org/10.1038/nature03805)
29. Oda, M., Iwashita, K.: *Mechanics Granular Materials, An Introduction*, 1st edn. Balkema, Rotterdam, Netherlands (1999)
30. Osher, S.J., Fedkiw, R.P.: *Level Set Methods and Dynamic Implicit Surfaces*, 1st edition. Springer, Berlin (2002)
31. Osher, S., Sethian, J.A.: Fronts propagating with curvature-dependent speed: algorithms based on hamilton-jacobi formulations. *J. Comput. Phys.* **79**, 12–49 (1988)
32. Pratt, W.K.: *Digital Image Processing*, 4th edn. Wiley, Los Altos (2007)
33. Rechemacher, A., Finno, R.: Digital image correlation to evaluate shear banding in dilative sands. *Geotech. Test. J.* **27**, 13–22 (2004)
34. Santamarina, J.C.: Soil behavior at the microscale: particle forces. In: *Proceedings of ASCE, Soil Behavior and Soft Ground, Construction*, pp. 25–56 (2003). doi:[10.1061/40659\(2003\)2](https://doi.org/10.1061/40659(2003)2)
35. Sheppard, A.P., Sok, R.M., Averdunk, H.: Techniques for image enhancement and segmentation of tomographic images of porous materials. *Phys. A: Stat. Mech. Appl.* **339**(1–2), 145–151 (2004). doi:[10.1016/j.physa.2004.03.057](https://doi.org/10.1016/j.physa.2004.03.057)
36. Soille, P.: *Morphological Image Analysis, Principles and Applications*, 2nd edn. Springer, Berlin (2004)
37. Sun, W., Andrade, J.E., Rudnicki, J.W., Eichhubl, P.: Connecting microstructural attributes and permeability from 3d tomographic images of in situ shear-enhanced compaction bands using multiscale computations. *Geophys. Res. Lett.* **38**, L10302 (2011a). doi:[10.1029/2011GL047683](https://doi.org/10.1029/2011GL047683)
38. Sun, W.-C., Andrade, J.E., Rudnicki, J.W.: Multiscale method for characterization of porous microstructures and their impact on macroscopic effective permeability. *J. Numer. Methods Eng.* **88**, 1260–1279 (2011b)
39. Thompson, K.E., Willson, C.S., Zhang, W.: Quantitative computer reconstruction of particulate materials from microtomography images. *Powder Technol.* **163**(3), 169–182 (2006). doi:[10.1016/j.powtec.2005.12.016](https://doi.org/10.1016/j.powtec.2005.12.016)
40. Vavrik, D., Soukup, P.: Metal grain structure resolved with table-top micro-tomographic system. *J. Instrum.* **6**, C11034 (2011). doi:[10.1088/1748-0221/6/11/C11034](https://doi.org/10.1088/1748-0221/6/11/C11034)
41. Vlahinić, I., Andrade, J.E., Andò, E., Viggiani, G.: From 3d tomography to physics-based mechanics of geomaterials. In: *Proceedings of ASCE, International Workshop in Computing in Civil Engineering*, pp. 339–345, Los Angeles, U.S. (2013)
42. White, J.A., Borja, R.I., Fredrich, J.T.: Calculating the effective permeability of sandstone with multiscale lattice boltzmann/finite element simulations. *Acta Geotech.* **1**, 195–209 (2006)
43. Zhao, H., Chan, T., Merriman, B., Osher, S.: A variational level set approach to multiphase motion. *J. Comput. Phys.* **127**, 179–195 (1996)